Modern Physical Chemistry Research (2024)
Clausius Scientific Press, Canada

DOI: 10.23977/mpcr.2024.040109
ISSN 2616-1702 Vol. 4 Num. 1

Core-shell rambutan-like nanoenzyme with oxidase-like activity for colorimetric detection of phenol

Peiqing Guo, Mingzhu Qiu, Xuefang Lei, Yujin Li, Xibin Zhou*

Key Laboratory of Resource Environment and Sustainable Development of Oasis, College of Geography and Environment Science, Northwest Normal University, Lanzhou, Gansu, 730070, China

**Corresponding author: zhouxb@nwnu.edu.cn*

Keywords: Nitrogen doped graphene quantum dots, Metal oxide, Colorimetric detection, Phenol, Nanozymes

Abstract: It is crucial to cultivate a a novel, convenient, and quick colorimetric approach to monitor phenol owing to its huge damage to people, biomass, and the environment. In this study, a rambutan-like nanocomposite $CuFe_2O_4$/N-GQDs@MnO_2 with the magnetic $CuFe_2O_4$ as the central core and MnO_2 as the outer shell was synthesized and highlighted. The introduction of nitrogen doped graphene quantum dots (N-GQDs) could not only alter the morphology of nanocomposite, but also link two different metallic oxides tightly. It is demonstrated that the materials prepared have good oxidase-like activity and can catalyze the coupling reaction of 4-aminoantipyrine (4-AAP) and phenol to yield a pink product in the absence of H_2O_2. Drawing upon this occurrence, a simple, low-cost, and highly selective colorimetric detection platform for phenol was developed. The instrument exhibits a linear response between 5μM and 200μM, with a sensitivity threshold of 0.18μM. In addition, the synthesized materials have good recyclability for the magnetism, indicating that $CuFe_2O_4$/N-GQDs@MnO_2 nanocomposites have great potential applications in the detection of phenol.

1. Introduction

Phenolic compounds, as common water pollutants, are highly toxic, hard to degrade, and a serious hazard to human health under natural conditions[1]. As a representative phenolic pollutant, phenol is widely found in the dyestuffs industry, manufacturing industries, plastics factories, and various petrochemical industries[2]. Since phenol can cause great harm to human health and the environment, and is a toxic pollutant even at low concentrations, the acceleration and accuracy of a method for determining phenol is of utmost importance[3]. Currently, traditional methods for the detection of phenol include chromatography, spectrophotometry, and chemiluminescence. Most of these methods are highly sensitive and reproducible. Nevertheless, professional operating staff, intricate sample pretreatment procedures, and exorbitant equipment have greatly limited their wide application[4]. The colorimetric method can be visually observed and compared with the naked eye according to the color alteration. It offers the benefits of economy, ease of use, and applicability. Nowadays, exploring various nanomaterials with excellent enzyme activity is still a hot topic in the

establishment of the colorimetric method.

In this work, we successfully synthesized rambutan-like $CuFe_2O_4$/N-GQDs@MnO_2 nanoparticles, with $CuFe_2O_4$ as the magnetic core and MnO_2 as the outer shell by a simple and environmentally friendly hydrothermal approach (as shown in Fig. 1). The materials prepared here exhibited strong oxidase-like activity to the chromogenic reaction of phenol 4-AAP. Furthermore, a rapid, accurate, and highly selective platform for phenol detection was established.

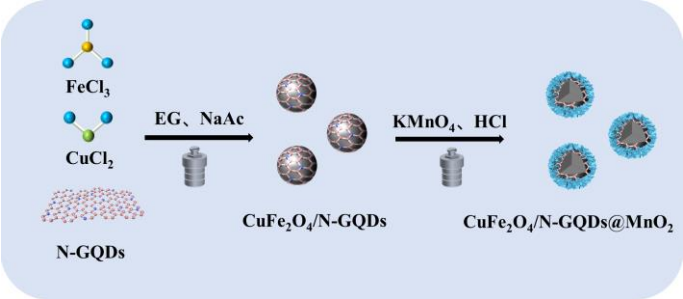

Figure 1: Graphical illustration of the creation process for $CuFe_2O_4$/N-GQDs@MnO_2

2. Experimental

2.1 Chemicals

Citric acid (CA), urea, $FeCl_3 \cdot 6H_2O$, $CuCl_2 \cdot 2H_2O$, ethylene glycol (EG), NaAc, potassium permanganate ($KMnO_4$), hydrochloric acid (37%, HCl), 3,3',5,5'-tetramethylbenzidine (TMB), o-phenylenediamine (OPD), H_2O_2, 4-aminoantipyrine (4-AAP), and phenol were sourced from Aladdin Chemical Co. The chemicals utilized were analytically pure and did not require further purification. Pure water of the highest grade was utilized throughout the entire process.

2.2 The preparation of N-GQDs

N-GQDs were synthesized on the basis of previous literature[5].

2.3 Preparation of $CuFe_2O_4$/N-GQDs nanoparticles

$CuFe_2O_4$/N-GQDs was formulated by a simple solvothermal method. To put it simply, 1.3g $FeCl_3 \cdot 6H_2O$, 0.4g $CuCl_2 \cdot 2H_2O$, and 2.0g NaAc were mixed with 30mL ethylene glycol and stirred for 15 min. Then, 0.8mL N-GQDs was slowly added to it, stirred for 30 min at 25 ℃ before being transferred into an 80 mL reaction still, which was heated in an oven at 200 ℃ for a duration of 12 h. Following a cooling period to ambient temperature, and the black sediment was gathered with magnets and repeatedly cleaned with ultrapure water and ethanol before being dried for 6h at 60 ℃.

2.4 Preparation of $CuFe_2O_4$/N-GQDs@MnO_2 magnetic nanocomposites

Magnetic composites were synthesized by a hydrothermal method. Typically, 0.5g $KMnO_4$ was first dissolved in 35mL ultrapure water, and then 0.7mL HCl (37wt%) was slowly added. After stirring for 15min, 0.3g $CuFe_2O_4$/N-GQDs was added and continued stirring for 15min. Finally, the blend was moved into an 80 mL Teflon-lined stainless steel autoclave reactor and heated in a 110℃ oven for 6h. After obtaining the product, the subsequent steps were carried out in the same manner.

2.5 Oxidase-like activity of $CuFe_2O_4$/N-GQDs@MnO_2 nanocomposites

The $CuFe_2O_4$/N-GQDs@MnO_2 exhibited oxidase-like activity through the catalytic oxidation of TMB. Generally, a mixture containing 50μL of $CuFe_2O_4$/N-GQDs@MnO_2 (18 mg/mL), 50μL of TMB (8 mM), and 1.9mL of NaAc-Hac buffer (0.2 M, pH 4) was prepared and permitted to stand at normal room temperature for a 5 min incubation period. Subsequently, absorbance readings were taken for the solution at 652 nm.

2.6 Characterization of ROS

The possible presence of reactive oxygen species (ROS) in the analogue enzymatic reaction was noticed by electron spin resonance (ESR).

2.7 Detection of phenol

Phenol detection was performed as follows: 150μL (18 mg/mL) $CuFe_2O_4$/N-GQDs@MnO_2 was dispersed in different concentrations of phenol solution, then 20μL (0.1 M) 4-AAP solution was added. After 20 min of reaction at ambient temperature, record data at 505 nm through magnetic separation.

2.8 Colorimetric assessment of water samples

The method's accuracy and applicability were confirmed through testing on real water samples. We selected tap water and Yellow River water to verify the practicability of the established method by calculating the recovery rate of the phenol spiked samples. The tap water was left untreated, while the Yellow River water underwent filtration through a 0.22 μm microporous membrane to eliminate coarse particulate impurities. The data presented here are the mean values obtained from three separate experiments.

3. Results and discussion

3.1 Analysis of $CuFe_2O_4$/N-GQDs@MnO_2

The size and morphology of $CuFe_2O_4$/N-GQDs@MnO_2 were analyzed by TEM. The image exhibits N-GQDs as particles with uniform morphology and good dispersion (Fig. 2A). The $CuFe_2O_4$/N-GQDs nanoparticles prepared by in-situ synthesis method are shown in Fig. 2B and 2C, which are regular spherical shape with particle diameter of about 200 nm. The results of $CuFe_2O_4$/N-GQDs@MnO_2 prepared by hydrothermal method are demonstrated in Fig. 2D. As can be seen from the picture, a thin layer of flower-like MnO_2 nanosheets was generated to encapsulate the spherical $CuFe_2O_4$/N-GQDs on the periphery of the spherical $CuFe_2O_4$/N-GQDs, forming a flower-like outer layer. Next, the element mapping analysis of the material was carried out. Fig. 2E shows that the prepared material contains C, N, O, Cu, Fe, and Mn elements, and the Mn element is evenly distributed around the entire $CuFe_2O_4$/N-GQDs core, pointing to a core-shell design $CuFe_2O_4$/N-GQDs@MnO_2 nanoparticles were successfully prepared. In addition, Fig. 2F shows $CuFe_2O_4$@MnO_2 nanoparticles. We can see that the diameter of the particles is larger without the addition of quantum dots, and the particles are more aggregated or even overlapped, and the dispersion is poor, which will seriously affect its catalytic efficiency. This phenomenon may be caused by the magnetic properties of the particles and the easy aggregation of MnO_2. Therefore, the addition of quantum dots was chosen to improve this problem. The surface of quantum dots

contains a great deal of hydroxyl groups. In the solvothermal environment characterized by elevated temperatures and pressures, the hydroxyl groups on the surface can generate electrostatic adsorption with metal cations, making metal ions relatively fixed, thus avoiding collision and agglomeration between them[6]. As shown in Fig. 2G, after the addition of quantum dots, the diameter of the prepared particles was significantly reduced and the contours were well-defined and more uniformly distributed. This demonstrates that the addition of N-GQDs can change their shape and size, resulting in an increase in their surface area and an increase in catalytically active sites. Fig. 2H shows the energy spectrum of the material, which further confirms the simultaneous presence of the elements C, N, O, Cu, Fe, and Mn. To sum up, it can be concluded that $CuFe_2O_4$/N-GQDs@MnO_2 has been successfully obtained.

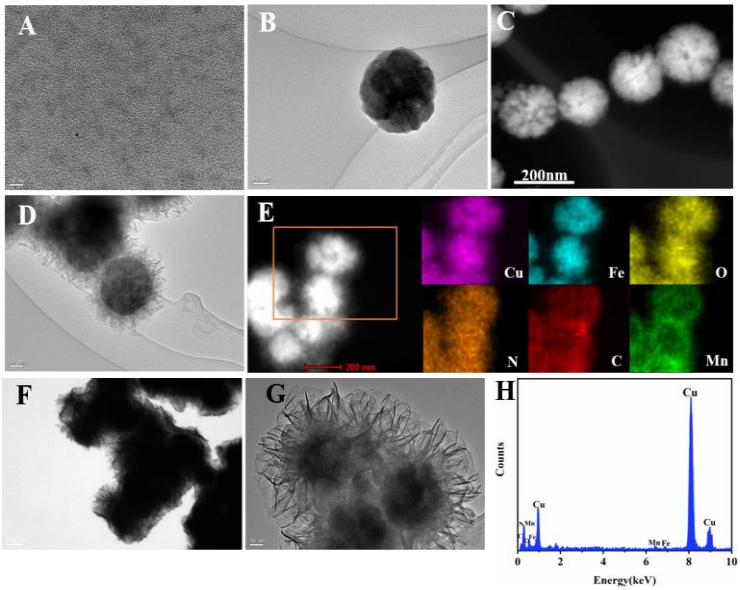

Figure 2: (A) TEM micrographs of N-GQDs; (B, C) $CuFe_2O_4$/N-GQDs; (D, G) $CuFe_2O_4$/N-GQDs@MnO_2; (E) Elemental mapping of $CuFe_2O_4$/N-GQDs@MnO_2; (F) $CuFe_2O_4$@MnO_2; (H) EDX pattern of $CuFe_2O_4$/N-GQDs@MnO_2

The nanocomposites' structure was investigated using XRD. As demonstrated in Fig. 3A, the diffraction patterns of $CuFe_2O_4$/N-GQDs nanoparticles display characteristic peaks at 2θ = 18.5°, 30.2 °, 35.5 °, 43.2 °, 53.6 °, 57.1 °, 62.7 °, and 74.2 °, aligning with the crystal faces of the spinel structure $CuFe_2O_4$ as indicated by the standard card (JCPDS 77-0010). These crystal faces are identified as (111), (220), (311), (400), (422), (511), (440) and (533)[7]. Besides, the peaks observed at 2θ = 12.8° and 37.6° correspond to the crystal plane reflections of (110) and (121), respectively, which can be associated with MnO_2 according to the standard card (JCPDS 72-1982)[8]. Contrasting the XRD patterns, no significant deviations are discernible, implying that the MnO_2 coating does not induce alterations in the lattice structure of the material. According to the XRD of $CuFe_2O_4$/N-GQDs@MnO_2, the diffraction peak of Cu^0 will be covered up after the coating of MnO_2, which indicates that core-shell $CuFe_2O_4$/N-GQDs@MnO_2 nanocomposites have been successfully prepared.

XPS was employed to delve into the surface properties and the elemental constituents. Fig. 3B illustrates the concurrent presence of C, N, O, Cu, Fe, and Mn elements. The XPS map focusing on the C 1s binding energy exhibits three fitted peaks attributed to the C=C (284.7 eV), C-O (286.1 eV), and O-C=O (288.9 eV) functional groups (Fig. 3C). The thorough spectrum in Fig. 3D exposes N 1s core, delineating three adjusted peaks at 398.9 eV, 399.8 eV, and 400.9 eV, signifying pyridine nitrogen, pyrrole nitrogen, and graphite nitrogen, severally[9]. As recorded in Fig. 3E, it is

characterized by three distinctive peaks, where 530.1 eV, 531.7 eV, and 532.7 eV correspond to Mn-O bond, oxygen in hydroxyl radical, and adsorbed oxygen, respectively. The Cu 2p XPS spectrum is depicted in Figure 3F, with binding energies of 932.6 eV and 954.8 eV for Cu $2p_{3/2}$ and Cu $2p_{1/2}$, severally. And Cu exists in two valence forms, Cu^0 (934.3 eV and 954.5 eV) and Cu^{2+} (935.8 eV and 952.6 eV). At the same time, the peak at 945.9 eV represents the satellite peak[10]. Besides, Fig. 3G depicts Fe 2p, with characteristic peaks at 711.4 eV and 719.6 eV belonging to Fe $2p_{3/2}$, and characteristic peaks at 725.1 eV and 732.1 eV assigned to Fe $2p_{1/2}$[11]. The Mn 2p spectrum, as displayed in Fig. 3H, exhibits distinctive peaks at 642.6 eV and 654.1 eV, matching the Mn $2p_{3/2}$ and Mn $2p_{1/2}$ peaks. individually. The separation in binding energies of the two peaks corresponds to 11.5 eV, which is roughly equivalent to that of pure MnO_2[12].

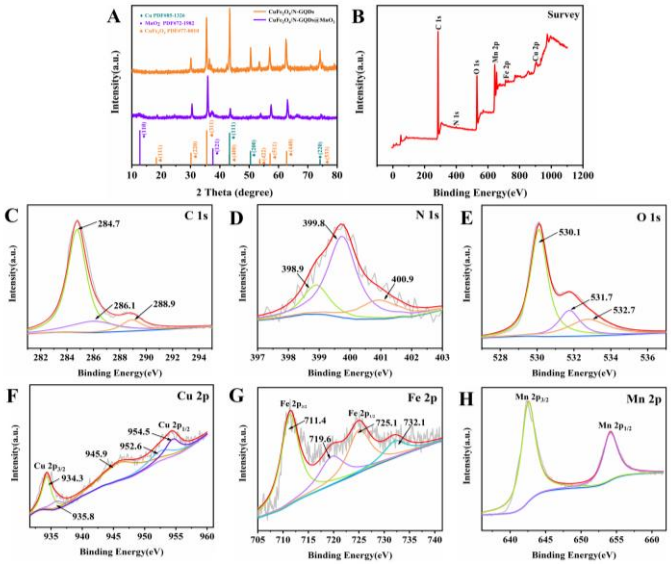

Figure 3: (A) XRD patterns of $CuFe_2O_4$/N-GQDs and $CuFe_2O_4$/N-GQDs@MnO_2; XPS spectra of $CuFe_2O_4$/N-GQDs@MnO_2: (B) Survey spectrum; (C) C 1s, (D) N 1s, (E) O 1s, (F) Cu 2p, (G) Fe 2p, and (H) Mn 2p.

The recyclable catalyst's magnetic properties facilitate the separation process, allowing for quick and efficient recovery. As shown in Fig. 4, the saturation magnetization is 33.52 emu/g, indicating that it has a high magnetic response. The catalyst can be separated from water within 30 seconds, which means that the catalyst exhibits a strong attraction towards the magnet, causing it to quickly migrate towards the magnet. Overall, the material's outstanding magnetic properties make it highly suitable for recyclable catalyst applications. Its strong magnetism ensures efficient recovery and separation, simplifying the process and allowing for repeated use of the catalyst.

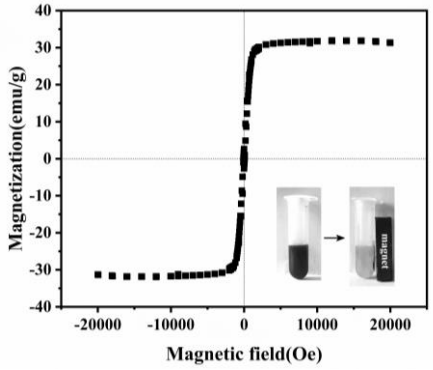

Figure 4: The magnetic hysteresis loops

3.2 Investigation of activity

To investigate the oxidase-like activity of $CuFe_2O_4$/N-GQDs@MnO_2, a series of experiments were next performed to assess oxidase-like activity. Among them, 8 mM TMB and o-phenylenediamine (OPD) were used as the substrates, 0.2 M NaAc-Hac (pH 4) buffer solution was used as reaction solution, and $CuFe_2O_4$/N-GQDs@MnO_2 nanomaterials were used as catalyst. Firstly, there is no absorption peak at 652nm in $CuFe_2O_4$/N-GQDs@MnO_2 solution and TMB solution alone (Fig. 5A). However, in the $CuFe_2O_4$/N-GQDs@MnO_2+TMB system, the absorbance of UV-vis spectra at 652nm was significantly enhanced, indicating that the material has good oxidase-like activity. At the same time, to compare its peroxide-like activity, 0.2 M H_2O_2 solution was added under the same reaction conditions. After adding it, the absorbance at 652nm is significantly lower than that of the solution without H_2O_2. Therefore, it is proved that the intrinsic oxide-like activity of the material is stronger than that of the peroxide-like activity, so its oxide-like activity was selected for follow-up experiments. In order to further demonstrate its activity, OPD, another typical chromogenic substrate, was replaced for experiments. From Fig. 5B, the system with OPD as the chromogenic substrate exhibits an obvious absorption peak at 450nm, which also indicates that it has an oxidase-like activity. Then, the systems were compared with $CuFe_2O_4$/N-GQDs@MnO_2 solutions. (Fig. 5C). As the concentration of the catalyst increases, the absorbance of system at 652nm also increases. After addition of sulfuric acid (Fig. 5D), the absorption peak at 652nm disappeared, proving that the reaction stopped. In summary, these results show that $CuFe_2O_4$/N-GQDs@MnO_2 nanomaterials exhibit good oxidase-like activity.

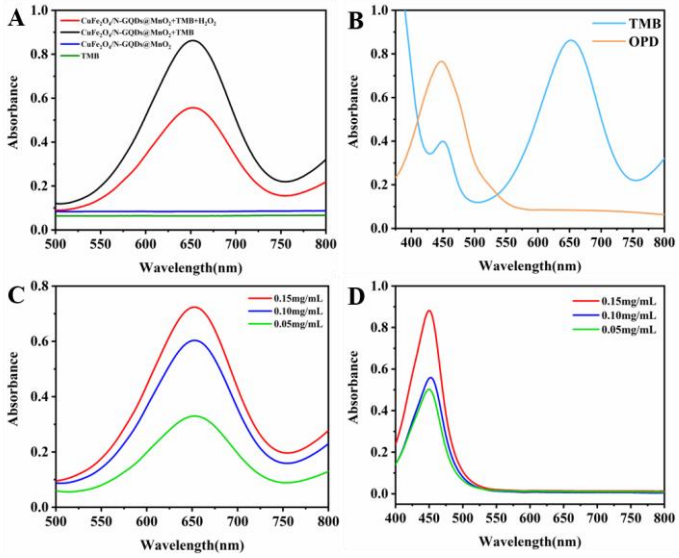

Figure 5: (A) UV-vis absorption profiles of TMB in diverse reaction environments; (B) The oxidation of diverse substrates facilitated by $CuFe_2O_4$/N-GQDs@MnO_2; (C) Varying concentrations of $CuFe_2O_4$/N-GQDs@MnO_2; (D) UV-vis spectra after adding sulfuric acid.

3.3 Investigation of reactive oxygen species.

In order to investigate the enzyme-like catalysis mechanism of $CuFe_2O_4$/N-GQDs@MnO_2, the generation of ROS was verified utilizing ESR spectroscopy. Reactive oxygen species usually refer to the free radicals present during the reaction, such as single linear $^1O_2$, •OH, and $•O_2^-$. DMPO and TEMP were selected as free radical scavengers to examine the free radicals produced during the reaction. According to the findings depicted in Fig. 6, the distinctive peaks corresponding to $^1O_2$, •OH, and $•O_2^-$ were detected. By comparing the signal intensity of the three radicals, it was possible

to conclude that the signal intensity of $\bullet O_2^-$ is much greater than that of $^1O_2$ and •OH. Therefore, it is suggested that $\bullet O_2^-$ is a key component in the detection process.

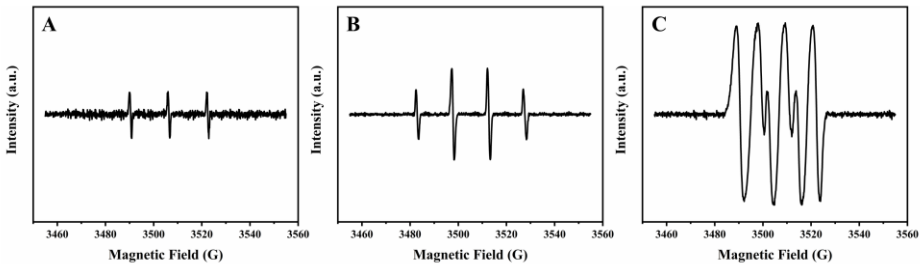

Figure 6: ESR spectra: (A) DMPO-•OH; (B) TEMP-$^1O_2$; (C) DMPO-$\bullet O_2^-$.

3.4 Colorimetric determination of phenol

Due to the excellent oxidase-like activity, a rapid and intuitive phenol detection platform has been constructed. As recorded in Fig. 7A, when phenol, 4-AAP, and the material coexisted, the color become noticeably pink, and the corresponding ultraviolet absorption spectrum exhibited a strong characteristic absorption peak at 505nm. The figure verifies the feasibility of the experiment. Fig. 7B is a schematic diagram of the mechanism for detecting phenol. In the original colorless system, due to the addition of $CuFe_2O_4$/N-GQDs@MnO_2, the 4-AAP and phenol was catalyzed to produce a pink quinone imine product. The catalytic mechanism of phenol detection was reasonably speculated: firstly, under the catalysis of the $CuFe_2O_4$/N-GQDs@MnO_2, the electron transfer rate was accelerated to generate quinoid radical and $\bullet O_2^-$. Subsequently, the active $\bullet O_2^-$ reacted with 4-AAP to shape antipyrine-•NH. Lastly, a pink quinone imine product would be produced by an oxidative coupling reaction between the quinoid radical and antipyrine-•NH.

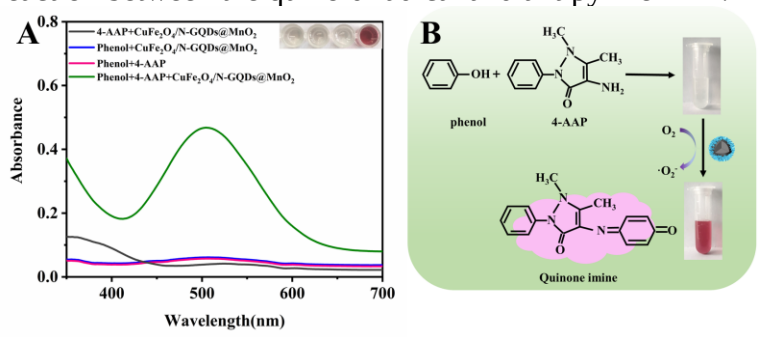

Figure 7: (A) UV–vis absorption characteristics across diverse systems; (B) Schematic illustration of $CuFe_2O_4$/N-GQDs@MnO_2 detection of phenol.

3.5 Refining the detection conditions

To attain the optimal performance for sensing, we conducted a thorough evaluation and optimization of a variety of reaction conditions. Generally, catalytic reactions require a certain reaction time to reach equilibrium. Hence, the optimization of reaction time was given priority to ensure the attainment of the best possible reaction outcomes. As Fig. 8A illustrated, absorbance measurements were taken at intervals of three minutes. It can be observed that after 21 minutes, the absorbance values remain relatively constant and exhibit a stable trend. Once the time was determined, the concentration of the optimized material was selected. During the process of optimizing the material concentration, it was found that the absorbance was increasing with the rise of the material concentration. Considering that the absorbance should be in accordance with the

Lambert-Beer law and the economy of the experiment, 0.18 mg/mL was chosen (Fig. 8B). In addition, various concentration of 4-AAP also significantly affects the efficiency of the reaction. According to Fig. 8C, with the increase of 4-AAP concentration, the trend of absorbance increases from fast to slow, so the concentration of 1mM is selected as the best concentration. The optimization of reaction temperature indicated that it is not greatly influenced by different temperatures (Fig. 8D), and room temperature was ultimately chosen for the subsequent experiments for the convenience of the experiment.

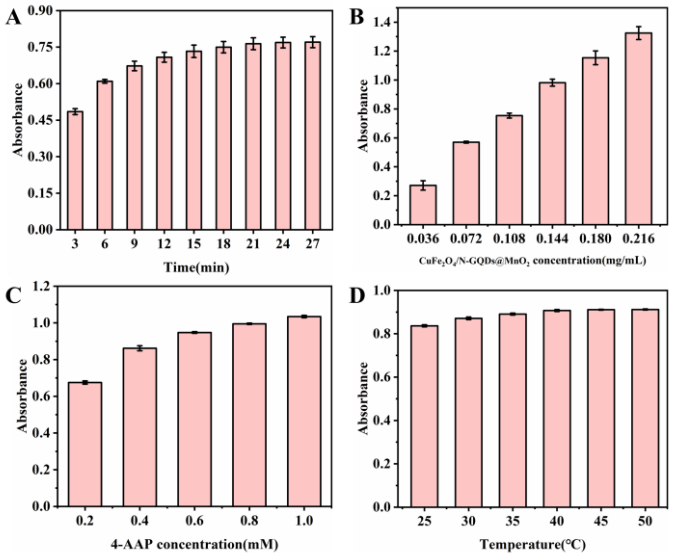

Figure 8: (A) Time; (B) A variety of concentration of $CuFe_2O_4$/N-GQDs@MnO_2; (C) A variety of concentration of 4-AAP; (D) Temperature.

3.6 Sensitivity of the system in identifying phenol

At the most favorable reaction conditions, different volumes of phenol solution were added to $CuFe_2O_4$/N-GQDs@MnO_2+4-AAP system. The reaction results were recorded by ultraviolet spectrophotometer. As the concentration of phenol increased, the absorption signal of the UV-vis spectrum at 505 nm also became stronger, and the solution's color gradually deepened, changing from light pink to dark pink (Fig. 9A). This phenomenon can be intuitively observed with the naked eye. As can be seen from Fig. 9B, the variation in absorbance levels the system at 505 nm (ΔA, $\Delta A=A-A_0$) presents a strong linear correlation within the concentration range of 5 to 200μM, R^2 is 0.992. It is calculated that the minimum detection limit of this method is calculated to be 0.18μM, is below the maximum allowable concentration of phenol in drinking water, as defined by regulations (0.2 mg/L).

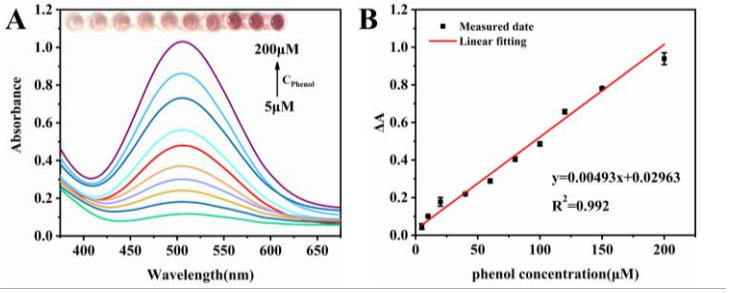

Figure 9: (A) UV-vis absorption characteristics in the presence of varying concentrations of phenol were obtained; (B) The linear relationship.

3.7 Selectivity and recovery performance

To evaluate specificity of protocol for the detection of phenol, multiple common organic molecules (2-methylimidazole, ethanol, acetone, cyclohexane, methanol, isopropanol, ethylene glycol, N, N-dimethylformamide, dimethyl sulfoxide) were controlled under other consistent conditions. These organic molecules were 20 times more concentrated than phenol, and their absorbance changes at 505 nm were recorded. In this colorimetric experiment, the absorbance of the other systems that were added with organic molecules was significantly lower than that of the systems added with phenol, except for the system that was added with phenol (Fig. 10A). The results showed that the detection platform was not susceptible to other organic molecules in the detection of phenol and had good selectivity. As a catalyst with magnetic properties, its reusability is essential. The reuse performance of $CuFe_2O_4$/N-GQDs@MnO_2 was tested by experiments. After each experiment, the material was separated using a magnet, and the material was subjected to several washes with ethanol and water, respectively, before moving on to the next experiment. Fig. 10B demonstrates its cycling performance. According to the image, its absorbance decreased significantly during the fourth experiment, indicating that the material possesses good repeatability for three cycles. Furthermore, the stability of the material was also investigated in Fig. 10C. After the material preparation was completed, the activity was measured every month. The experimental results show that the absorbance of $CuFe_2O_4$/N-GQDs@MnO_2 does not decrease significantly within 6 months, indicating that the prepared material has good stability.

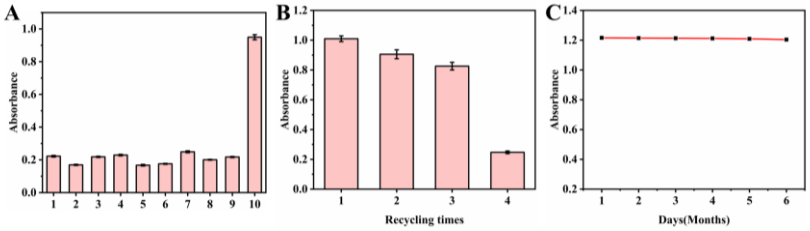

Figure 10: (A) Assessment of the selectivity (1. 2-methylimidazole; 2. ethanol; 3. acetone; 4. Cyclohexane; 5. Methanol; 6. Isopropanol; 7. ethylene glycol; 8. N, N-dimethylformamide; 9. dimethyl sulfoxide); (B) Catalysis cycles; (C) Material stability within six months.

3.8 Determination of phenol in real samples

With the aim of verify that the method has certain practical value, the phenol content was evaluated in tap water and Yellow River water. Given the substantial presence of sediment in it, strategies were taken to eliminate insoluble impurities by subjecting the collected water to filtration using a 0.22μm microporous filter membrane. The tap water was kept untreated. No phenol was detected among them, so the standard addition method was used. As shown in Table 1, the recovery rate of this method is between 95.34% and 104.67%. The results show that this approach can be used to determine the presence of phenol in the environment and has good sensitivity and accuracy for real samples.

Table 1: Findings from the analysis of phenol content in actual samples.

	Spiked/μM	Found/μM	Recovery/%	RSD/%
Tap-water	50	51.87	103.73	1.23
	100	98.86	98.86	2.54
	200	209.34	104.67	0.23
Yellow River	50	51.06	102.11	4.24
	100	95.34	95.34	3.11
	200	197.71	98.85	2.69

4. Conclusions

In conclusion, rambutan-like nanocomposites $CuFe_2O_4$/N-GQDs@MnO_2 with core-shell structure were successfully synthesized for the first time by using simple hydrothermal method, and used for colorimetric detection of phenol. The incorporation of N-GQDs not only changes the morphology, but it also enhances the binding effect with metal ions due to the surface functional group, which results in better oxidase-like activity. The established technique demonstrated a broad linear response range, a minimum detection threshold, and superior selectivity in the identification of phenol. Furthermore, the magnetic properties of the materials make them more convenient to handle and reuse, thereby avoiding environmental pollution.

Acknowledgements

The authors acknowledge the National Natural Science Foundation of China (21165016, and 21265018); the Science and Technology Support Projects of Gansu Province (No.s 1011GKCA025, and 1208RJZM289).

References

[1] Hou C, Fu L, Wang Y, et al. Co-MOF-74 based Co_3O_4/cellulose derivative membrane as dual-functional catalyst for colorimetric detection and degradation of phenol. Carbohydrate Polymers, pp. 273, 2021.

[2] Gao J, Liu M, Song H, et al. Highly-sensitive electrocatalytic determination for toxic phenols based on coupled cMWCNT/cyclodextrin edge-functionalized graphene composite. Journal of Hazardous Materials, no. 318, pp. 99-108, 2016.

[3] Wang Y, Han X, Xu P, et al. Synthesis of pomegranate-like Mo_2C@C nanospheres for highly efficient microwave absorption. Chemical Engineering Journal, no. 372,pp. 312-320, 2019.

[4] Bai D, Xue Z, Guo P, et al. Ultrasensitive colorimetric detection of Hg^{2+} based on glutathione-modified Au nanoflowers. Microchemical Journal, pp. 181, 2022.

[5] Qu D, Zheng M, Du P, et al. Highly luminescent S, N co-doped graphene quantum dots with broad visible absorption bands for visible light photocatalysts. Nanoscale, vol.5, no. 24, pp. 12272-12277, 2013.

[6] Yang Y, Liu Q, Liu Y, et al. A novel label-free electrochemical immunosensor based on functionalized nitrogen-doped graphene quantum dots for carcinoembryonic antigen detection. Biosensors and Bioelectronics, no. 90, pp. 31-38, 2017.

[7] Darvish M, Nasrabadi N, Fotovat F, et al. Biosynthesis of Zn-doped $CuFe_2O_4$ nanoparticles and their cytotoxic activity. Sci Rep, vol.12, no. 1, pp. 9442, 2022.

[8] Zhang H, Yao S, Zhao C, et al. Feasibility Study on Facile and One-step Colorimetric Determination of Glutathione by Exploiting Oxidase-like Activity of Fe_3O_4-MnO_2 Nanocomposites. Analytical Sciences, vol.37, no. 10, pp. 1355-1360, 2021.

[9] Shao T, Zhang Q, Li J, et al. AgPt hollow nanodendrites based on N doping graphene quantum dots for enhanced methanol electrooxidation. Journal of Alloys and Compounds, pp. 882, 2021.

[10] Dong Y, Chui Y-S, Ma R, et al. One-pot scalable synthesis of Cu–$CuFe_2O_4$/graphene composites as anode materials for lithium-ion batteries with enhanced lithium storage properties. Journal of Materials Chemistry A, vol. 2, no. 34, 2014.

[11] Shu R, Zhao Z, Yang X. Synthesis of hollow $CuFe_2O_4$ microspheres decorated nitrogen-doped graphene hybrid composites for broadband and efficient electromagnetic absorption. Journal of Colloid and Interface Science, no. 648, pp. 66-77, 2023.

[12] Zhou Q, Ma S, Zhan S. Superior photocatalytic disinfection effect of Ag-3D ordered mesoporous CeO_2 under visible light. Applied Catalysis B: Environmental, no. 224, pp. 27-37, 2018.